Simulation of Cold Flow in a Truncated Ideal Nozzle with Film Cooling

Kalen Braman[1]
Tuskegee University, Jacobs ESSSA Group, NASA Marshall Space Flight Center, Huntsville, AL 35812, USA

Joseph Ruf[2]
NASA Marshall Space Flight Center, Huntsville, AL 35812, USA

Flow transients during rocket start-up and shut-down can lead to significant side loads on rocket nozzles. The capability to estimate these side loads computationally can streamline the nozzle design process. Towards this goal, the flow in a truncated ideal contour (TIC) nozzle has been simulated using RANS and URANS for a range of nozzle pressure ratios (NPRs) aimed to match a series of cold flow experiments performed at the NASA MSFC Nozzle Test Facility. These simulations were performed with varying turbulence model choices and for four approximations of the supersonic film injection geometry, each of which was created with a different simplification of the test article geometry. The results show that although a reasonable match to experiment can be obtained with varying levels of geometric fidelity, the modeling choices made do not fully represent the physics of flow separation in a TIC nozzle with film cooling.

Nomenclature

NPR	=	nozzle pressure ratio, Pc/Pamb
Pc	=	chamber pressure
Pamb	=	ambient pressure
Pw	=	wall surface pressure
r*	=	nozzle throat radius

I. Introduction

THE design of new rocket nozzles or the use of existing designs in new configurations requires the estimation of nozzle transient effects such as occur during start-up and shut-down. These transients can cause significant side loads on the nozzle. The relative magnitude of these side loads for different types of nozzle contours can be estimated with subscale cold flow experiments. However, determining the absolute magnitudes of nozzle side loads requires full scale hot fire tests. These hot fire tests can be costly with regards to both money and time, especially if design problems are not discovered until the full scale tests. Therefore, a computational tool which can predict these transient effects can greatly streamline the design and test cycle.

An accurate prediction of the nozzle side loads requires an accurate prediction of the flow separation location within the nozzle. Furthermore, the separation location can be affected by nozzle modifications, like the film cooling systems applied to some radiatively cooled nozzles[1]. Thus a computational tool capable of accurately predicting nozzle flow separation must be able to account for these nozzle modifications.

This paper addresses the computational modeling requirements necessary to predict the effects of nozzle film cooling on the surface pressures and flow separation location in a nozzle. Focus of this work includes the simplifications applied to the computational geometry, as well as the turbulence modeling choices made, and how these affect the surface pressure and separation location accuracy. To facilitate the discussion of solution accuracy, a nozzle with corresponding experimental results was selected. Specifically, the nozzle geometry aims to match that used during a series of cold flow nozzle experiments performed at the NASA MSFC Nozzle Test Facility (NTF)[2,3]. In this set of experiments, the nozzle pressure ratio (NPR) was stepped through a range of stationary values by decreasing

[1] Combustion Instability and Fluids Analyst, Jacobs ESSSA Group, ER42, NASA MSFC, AL 35812
[2] ER42, NASA MSFC, AL 35812

the facility back pressure. The aim is to show what level of geometry simplifications and which turbulence modeling choices provide reasonable accuracy in determining surface pressures and separation location.

II. Methodology

A. Model Geometry

The simulation models were derived from a truncated ideal contour (TIC) nozzle geometry[2,3]. The nozzle geometry includes an annular slot in the diverging section, the 'nozzlette', which provides an auxiliary supersonic flow injection for film cooling. Figure 1 shows a schematic of the nozzle and nozzlette. A more detailed view of the nozzlette is shown in Fig. 2.

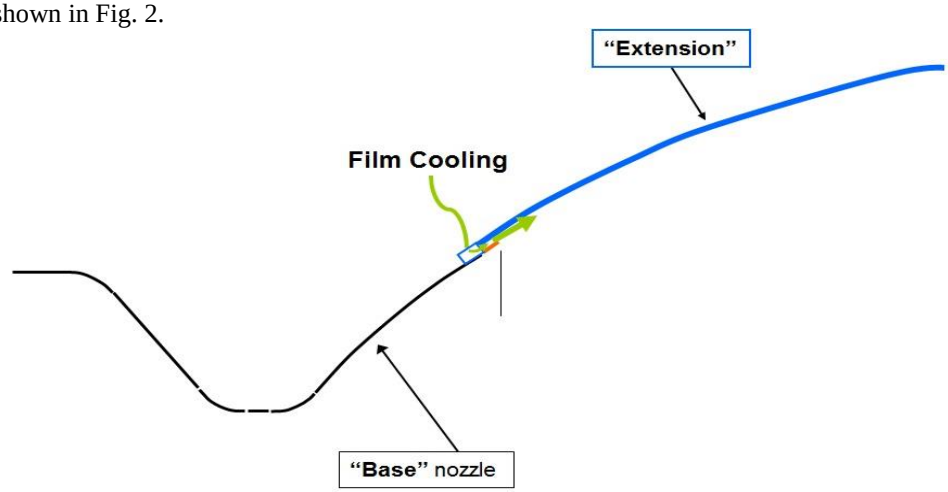

Figure 1: Schematic of the TIC nozzle contour with the film cooling nozzlette

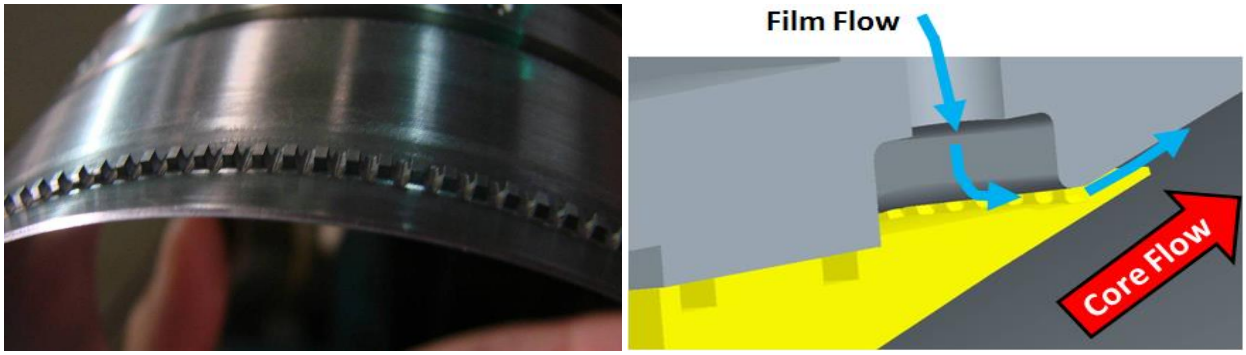

Figure 2: The nozzlette geometry with an upstream view of the actual hardware (left) and an isometric view of the manifold and nozzlette orifice (right)

One axisymmetric and three different three-dimensional mesh configurations were created to approximate the nozzlette geometry. The computational domains of the three three-dimensional configurations span a single tooth/channel section azimuthally. The four different mesh configurations, shown in Fig. 3 as detailed wireframe views of the nozzlette, aimed to determine the sensitivity of the simulation results to the approximations made in defining the computational model geometries and computational meshes. Additional computational meshes were created to test mesh density effects but were not included in the tally of four.

The axisymmetric mesh uses an equivalent slot area to mimic the effect of the flow blockage caused by the teeth, since the orifice teeth cannot be created in an axisymmetric mesh. The three-dimensional meshes were created primarily by extrusion of the axisymmetric mesh. The regions of extrusion are labeled in Fig. 4 to show which portions of the domain were or were not extruded for the three-dimensional meshes. The first of the three three-dimensional computational meshes, labeled 3D_twoD_tooth, was created by rotationally extruding the majority of the axisymmetric mesh. The portion not rotationally extruded, a region that extends the length of the domain near the nozzle centerline, was axially extruded from the nozzle inlet. After the extrusions, the two periodic planes of 3D_twoD_tooth match exactly the axisymmetric mesh. Like the axisymmetric mesh, this mesh contains none of the

orifice teeth, but instead contains an obstruction which extends rotationally around the orifice. The second three-dimensional mesh, labeled 3D_sqr_tooth, again was created by the same extrusions, except for the nozzlette tooth region. For this mesh, the rounded tooth design of the TIC nozzlette geometry was simplified with a squared tooth design. The squared tooth design aimed to provide three-dimensional blockage to the nozzlette flow equivalent to that anticipated with a rounded tooth while maintaining the ability to use a structured mesh in the nozzlette orifice region. The final three-dimensional mesh, labeled 3D_rnd_tooth, includes a tooth and channel which match the as-designed TIC nozzlette. The rest of the domain again was created by two extrusions. The bulk of the computational domain of these last two meshes match exactly mesh 3D_twoD_tooth. The differences are only in the nozzlette region.

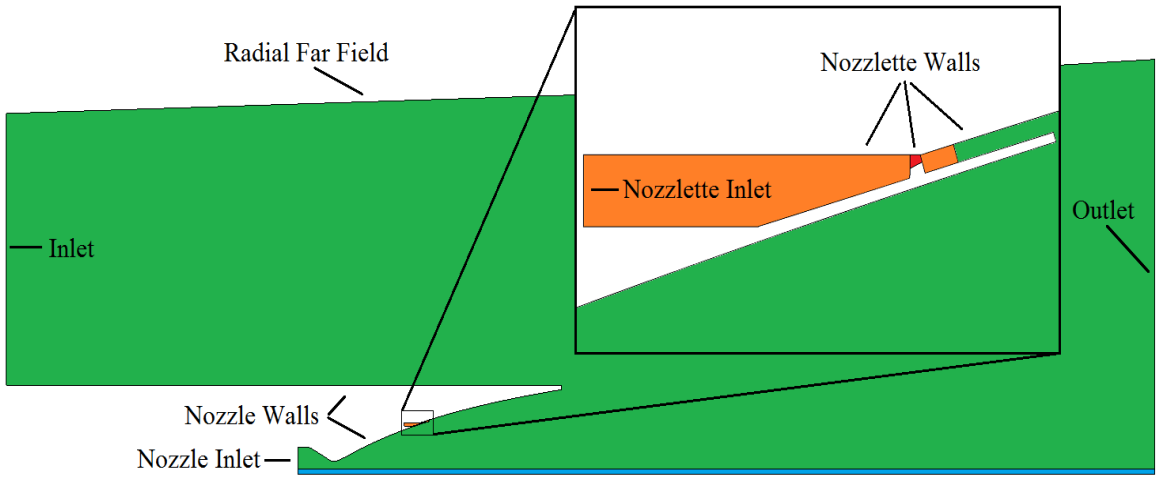

Figure 3. Regions of extrusion in the 3D meshes: blue – axial extrusion for all 3D meshes, green – rotational extrusion for all 3D meshes, orange – rotational extrusion for 3D_twoD_tooth and 3D_sqr_tooth, and red – rotational extrusion for 3D_twoD_tooth only; also labeled are the boundaries

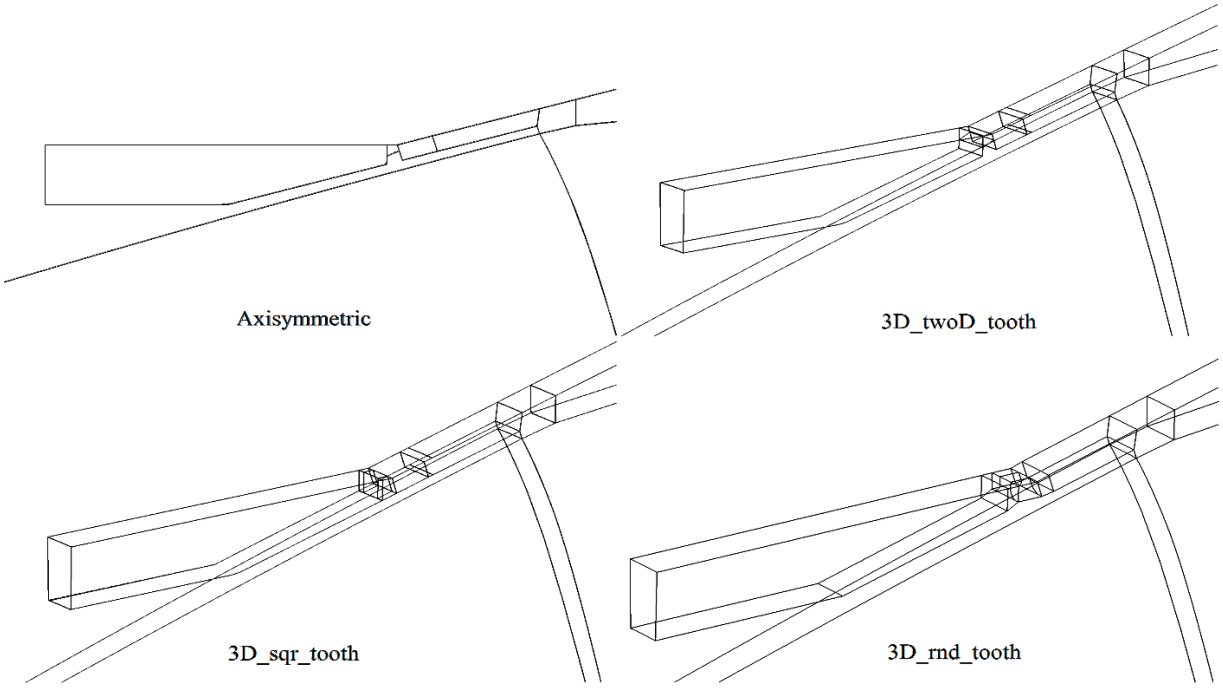

Figure 4. Axisymmetric and three-dimensional geometry for the nozzlette region shown in wireframe

B. Simulation Methodology

The simulations were performed to steady state using Loci/CHEM. Loci/CHEM[4-6] is a density-based finite-volume CFD program built upon the Loci[7,8] framework. For the axisymmetric mesh configuration, the simulations

were stepped forward through NPR using the result of the previous NPR's simulation as the initial condition. For each three-dimensional mesh configuration, the simulation started using the corresponding axisymmetric steady solution as the initial condition. For some of the three-dimensional simulations, the solutions did not reach a converged state as steady state simulations. For those simulations, a time accurate simulation was performed using the unconverged steady solution as the initial condition. Once the simulations reached a stationary state, the solutions were time-averaged to obtain the wall pressure results. The turbulence models included in this investigation are Menter's baseline (BSL)[9,10] and Menter's Shear Stress Transport (SST)[9,10] models, and the compressibility corrections are the Wilcox correction[11] and a modified version of the Sarkar correction[12], here labeled Sarkar*.

III. Results

The simulations presented here aim to approximate a set of experiments performed at the MSFC NTF[2,3]. In the experiments, warmed dry air was delivered to the test article. Experiments were conducted over a range of NPRs by varying the pressure in the test cell through the use of an ejector system. Two nozzlette flow rates are documented here, no film flow and supersonic film flow. For each film flow rate and each mesh configuration, a set of simulations were performed at increasing values of NPR, which was accomplished by dropping the ambient pressure.

The experimental measurements included a dense array of static pressures along the nozzle surface[2,3]. These measurements of pressure allow the determination of the flow separation location along the nozzle wall. Thus, the primary quantities of interest for the simulations are the nozzle surface pressures and the locations of separation. For the remainder, the surface pressure distributions will be reported normalized by chamber pressure and plotted versus axial distance normalized by the nozzle throat radius r*.

C. Axisymmetric Results

Results for the axisymmetric mesh were computed for a set of turbulence modeling choices which are listed in Table 1. Each of these selections was performed for both film flow cases, no nozzlette flow and supersonic nozzlette flow. Figures 5 and 6 display the pressure profiles for no nozzlette flow and supersonic nozzlette flow, respectively. Simulation results for NPR 15 are shown in Fig. 5, although no experimental data was collected for that NPR with no nozzlette flow. Also, for no nozzlette flow, NPR 67 was the closest available experimental data to NPR 70, which was reported for supersonic nozzlette flow.

Table 1: Turbulence model selections for the axisymmetric simulations

Case	Turbulence model	Compressibility correction
A1	BSL	Sarkar*
A2	BSL	Wilcox
A3	SST	Sarkar*
A4	SST	Wilcox

For no nozzlette flow (Fig. 5), case A1 which uses Menter's BSL turbulence model and the modified Sarkar compressibility correction generally matches the experimental results the closest, particularly at higher NPRs. The other three model combinations show early separation for NPRs 67, 90, and 120, whereas A1 matches the separation location very closely for NPR 120 and shows slightly late separation for NPRs 67 and 90. The experimental separation location is not available for NPRs 40 and 50 because pressure taps could not be placed in the vicinity upstream of the nozzlette. However, at those two NPRs, the wall pressures downstream of the separation location (for most cases) match the experimental results reasonably well. The largest discrepancy is for case A1 in the region just downstream of the nozzlette.

For the cases with supersonic nozzlette flow (Fig. 6), both A1 and A2 tend to match the experimental results the closest. The separation locations for A2 tend to occur upstream of the A1 separation locations, and the experimental separation locations tend to lie in between those from A1 and A2 (excluding NPRs 40 and 50 for which no experimental separation location can be determined). The other two model combinations A3 and A4 show early separation for every NPR for which an experimental separation location can be determined (15, 67, 90, and 120). Additionally, for all model combinations, the wall pressures in the extension nozzle at locations upstream of separation tend to be slightly higher than the experimental values. This behavior was not seen in the cases with no nozzlette flow.

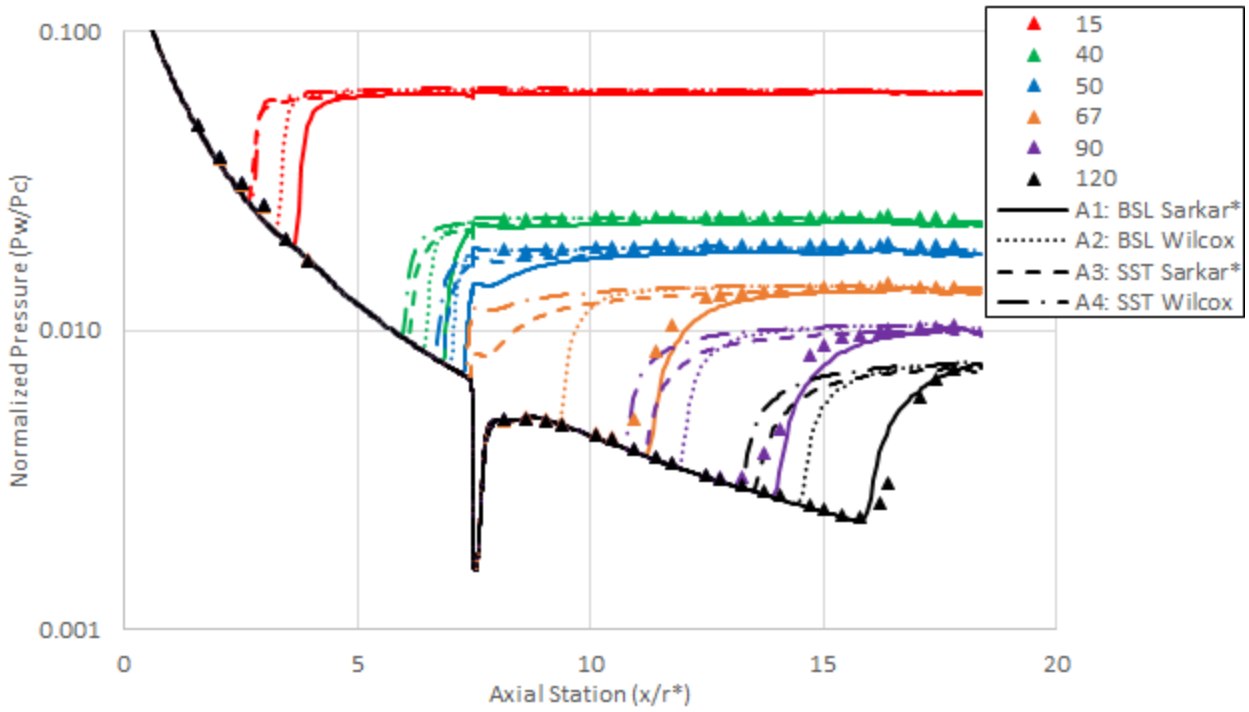

Figure 5: Non-dimensional pressure profiles for the axisymmetric mesh with no nozzlette flow with case A1 solid lines, case A2 dotted lines, case A3 dashed lines, and case A4 long dashed lines, plotted against the experimental results in symbols

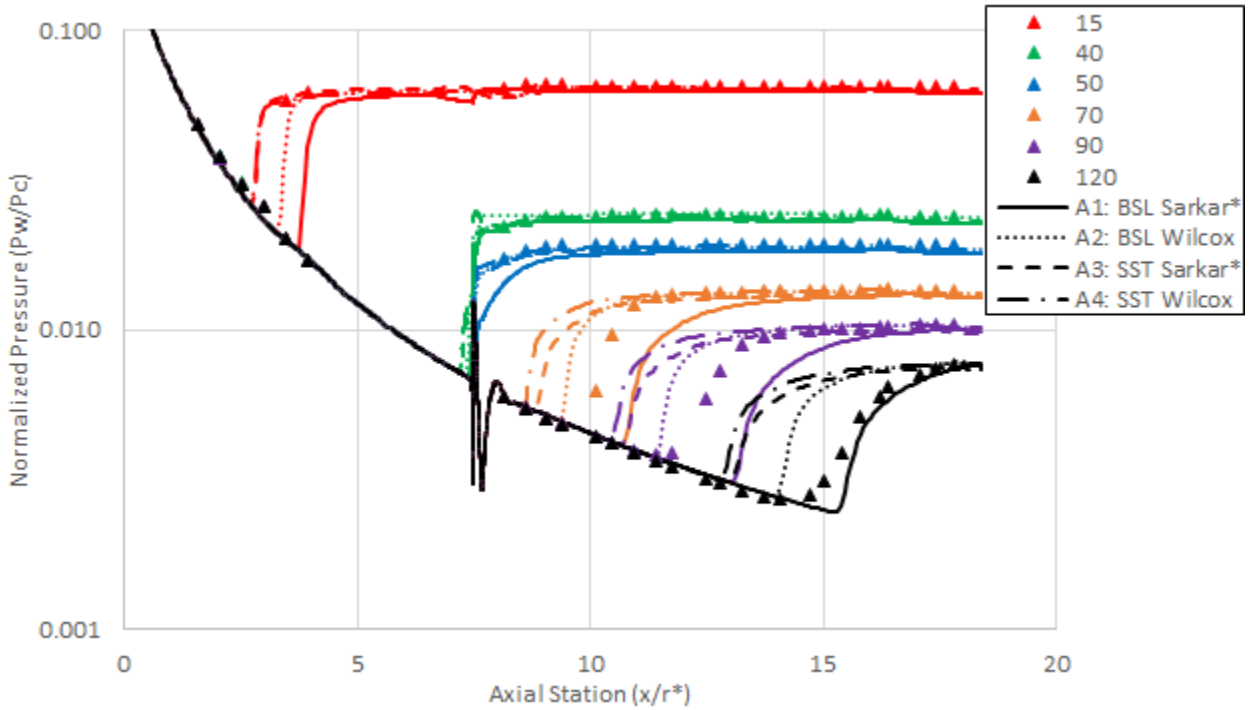

Figure 6: Non-dimensional pressure profiles for the axisymmetric mesh with supersonic nozzlette flow with case A1 solid lines, case A2 dotted lines, case A3 dashed lines, and case A4 long dashed lines, plotted against the experimental results in symbols

From these axisymmetric results, Menter's Baseline turbulence model appears to produce surface pressures and separation locations which match experiment more closely than Menter's Shear Stress Transport turbulence model.

Additionally, although the modified Sarkar correction leads to separation locations closer to experimental results for the no nozzlette flow case, the results are not as close for the with nozzlette flow case. For the case with nozzlette flow, the results using the Wilcox and modified Sarkar corrections appear to bound the experimental separation locations for the available NPRs. Therefore, only Menter's Baseline turbulence model was used for the three-dimensional cases which are discussed in the following section.

D. Three-dimensional Results

Results for the three-dimensional meshes were computed only for the cases which include supersonic nozzlette flow and not for the cases with no nozzlette flow. The results are reported for two turbulence model and compressibility correction combinations, Menter's BSL model with the modified Sarkar compressibility correction and Menter's BSL model with the Wilcox correction. Those two combinations provided the closest match to experiment for the axisymmetric results, and also appeared to bound the separation location over the investigated range of NPR. The results for the three-dimensional meshes are displayed against the corresponding axisymmetric results and the experimental data in Fig. 7 to Fig. 12.

Figure 7 shows the results for the modified Sarkar compressibility correction. For NPR 15 where the separation occurred well upstream of the nozzlette exit, all mesh configurations produce almost the same separation location (within 0.1 r*). For NPR 40 all mesh configurations indicate the separation location was at or slightly upstream of the nozzlette exit.

For clarity, Fig. 8 and Fig. 9 show only a portion of the NPRs for the results for the modified Sarkar correction. At NPR 40 (Fig. 8) the axisymmetric and 3D_twoD_tooth wall pressures are nearly the same; however, the 3D_rnd_tooth and particularly 3D_sqr_tooth wall pressures more gradually rise until matching the experimental wall pressures further down in the nozzle extension. At NPR 50 (Fig. 9) the separation location for the axisymmetric and 3D_twoD_tooth agree closely as expected given that the 3D_twoD_tooth mesh is the three-dimensional wedge equivalent of the axisymmetric mesh. The separation location for the 3D_sqr_tooth remains at the nozzlette exit agreeing with the axisymmetric and 3D_twoD_tooth results. On the other hand, the separation location for the 3D_rnd_tooth (x/r* of 9.3) is well downstream of the test data.

At NPR 70 (Fig. 8) the separation locations produced by the different configurations are all different and spaced roughly evenly apart over a range of 0.8 r*. Of the four configurations, the 3D_twoD_tooth comes closest to matching the test data, but is approximately 0.7 r* downstream. At NPR 90 (Fig. 9) the simulations' separation locations from the four configurations return to being similar but are well downstream of the test data. At NPR 120 (Fig. 8) the simulations' separation locations remain similar, but with improving agreement with the test data. Across this set of NPRs, the axisymmetric and 3D_twoD_tooth separation locations were similar, with the 3D_twoD_tooth locations tending to be slightly upstream of those from the axisymmetric mesh.

Figure 10 shows the results for the Wilcox compressibility correction. Like with the modified Sarkar compressibility correction, for NPR 15 where the separation occurred well upstream of the nozzlette exit, all mesh configurations produce the same separation location. Again for NPR 40 all configurations indicate the separation location was at or slightly upstream of the nozzlette exit.

Figure 11 and Fig. 12 show a selection of the NPRs in order to provide a clearer picture of the surface pressure and separation location results. At NPR 40 (Fig. 11), the pressures for 3D_twoD_tooth and 3D_rnd_tooth both match experiment closely, while the results for the axisymmetric model show a slight overshoot in pressure just past the nozzlette outlet and the results for the 3D_sqr_tooth show an underestimation of pressure for about 2 r* downstream of the nozzlette. At NPR 50 (Fig. 12), by 0.5 r* downstream of the nozzlette exit, the pressures for all four models match. For all experimental measurement locations along the nozzle extension, the simulation results match the experiments closely.

At NPR 70 (Fig. 11), the axisymmetric and 3D_twoD_tooth results, which again match within a small margin as expected since the three-dimensional model is a wedge version of the axisymmetric, show separation locations upstream of the experimental separation. The 3D_sqr_tooth and 3D_rnd_tooth separation locations are 0.7 and 1.0 r* downstream of the other two models, though the 3D_sqr_tooth pressure values are very close to the experimental data. At NPR 90 (Fig. 12), the pressure results for 3D_sqr_tooth and 3D_rnd_tooth tend to be closer to experiment, though the separation locations for all configurations are within about 0.3 r* of the experimental value. Finally, at NPR 120 (Fig. 11), the pressure results for all configurations fall nearly on top of each other upstream of the experimental separation location.

It was expected that the additional fidelity included by modeling the three-dimensional features of the film orificing (the 3D_sqr_tooth and 3D_rnd_tooth meshes) would improve the simulations' flow separation locations. However, as shown in Fig. 7 to Fig. 12, this was not strictly the case for Menter's Baseline turbulence model with either compressibility correction. For instance, the separation locations for the modified Sarkar correction at NPR 70

are significantly further downstream of those from the lower fidelity models and the experimental data. For the Wilcox compressibility correction, although at NPRs 70 and 90 the 3D_sqr_tooth and 3D_rnd_tooth show better agreement with experiment versus the axisymmetric and 3D_twoD_tooth results, the two meshes with three-dimensional features do not show this improvement universally across NPR. The fit at NPRs 70 and 90 is likely due to coincidence as opposed to capturing of all the relevant physics. The comparison of these results for all mesh configurations versus experiment indicates that in addition to nozzlette orifice geometry, some other factor not captured in these models is affecting the nozzlette flow and ultimately the nozzle flow separation location. Nonetheless, regardless of the separation location, the portion of the pressure profiles in the separated flow region matched the experiments closely for all simulations. Also, no matter the selected compressibility correction, upstream of the nozzlette location and far downstream of the nozzlette location the results for all geometric configurations nearly collapse for each compressibility correction.

Although the meshes were designed with the same orifice area and the same stagnation pressure was used for the film inlet, the resultant nozzlette mass flow varied between the different mesh configurations. This variation occurred due to different effective constriction of the nozzlette flow caused by the different three-dimensional orificing. As a result, the film injection mass flow varied from the experimental value by as much as 8%. This mismatch in the film injection mass flow rate has a minor impact on the quantities of interest. Adjustments to the nozzlette stagnation pressure for NPR 50 to match the experimental film flow rate resulted in only minor changes to the separation location (a shift of less than 0.1 r*) and no change in the trend amongst meshes. It is expected that the variation in film mass flow in these simulations does not significantly affect the results at other NPRs.

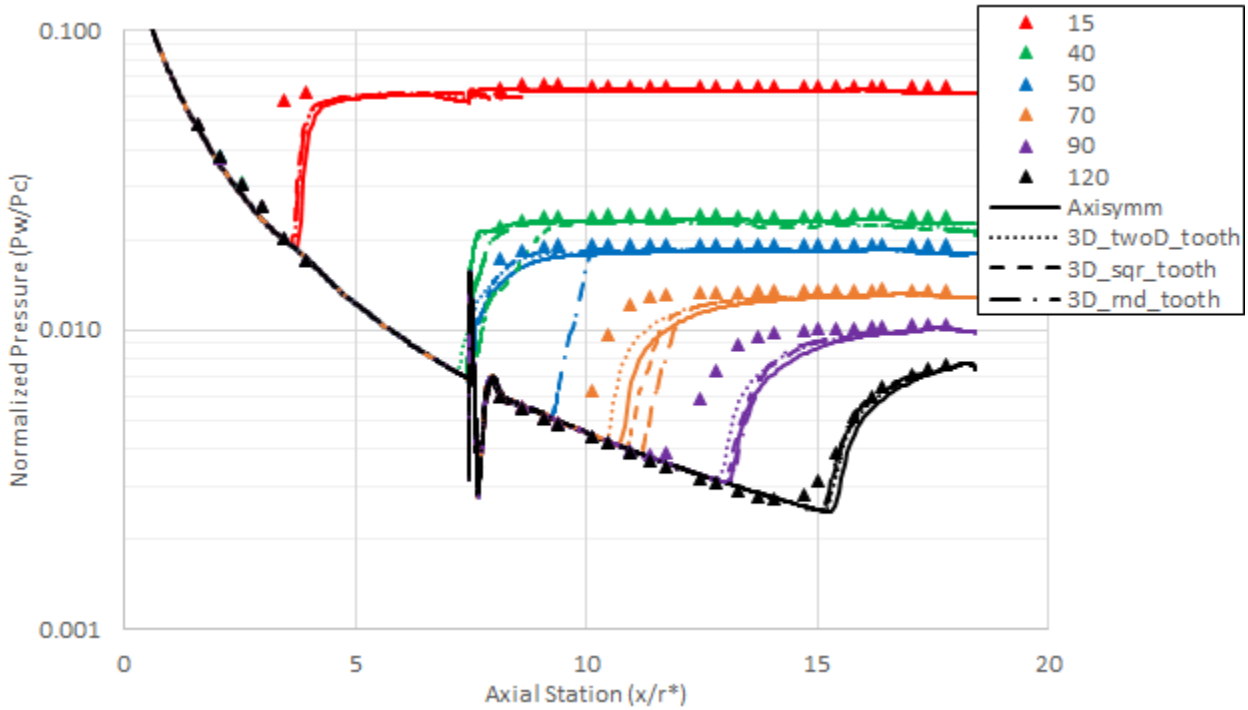

Figure 7. Non-dimensional pressure profiles at various NPR for all mesh configurations (lines) using Menter's BSL model and Sarkar* compressibility correction plotted against the experimental results (symbols)

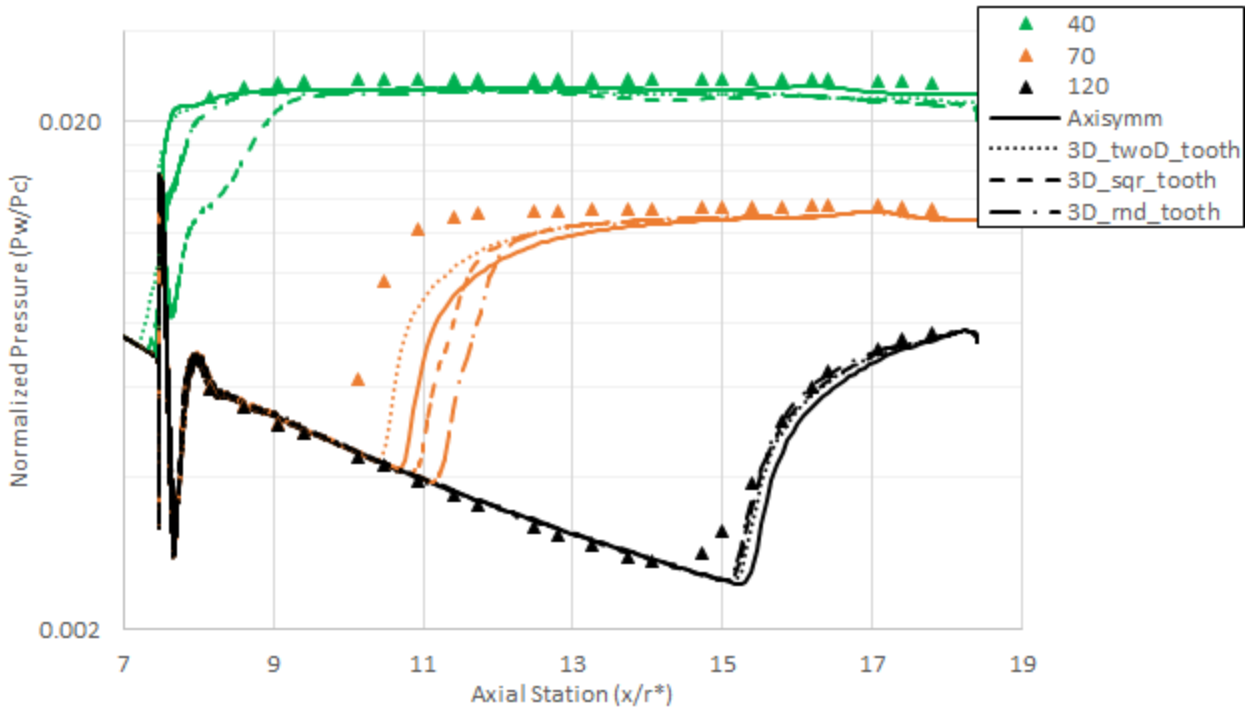

Figure 8. Non-dimensional pressure profiles at NPRs 40, 70, and 120 for all mesh configurations (lines) using Menter's BSL model and Sarkar* compressibility correction plotted against the experimental results (symbols)

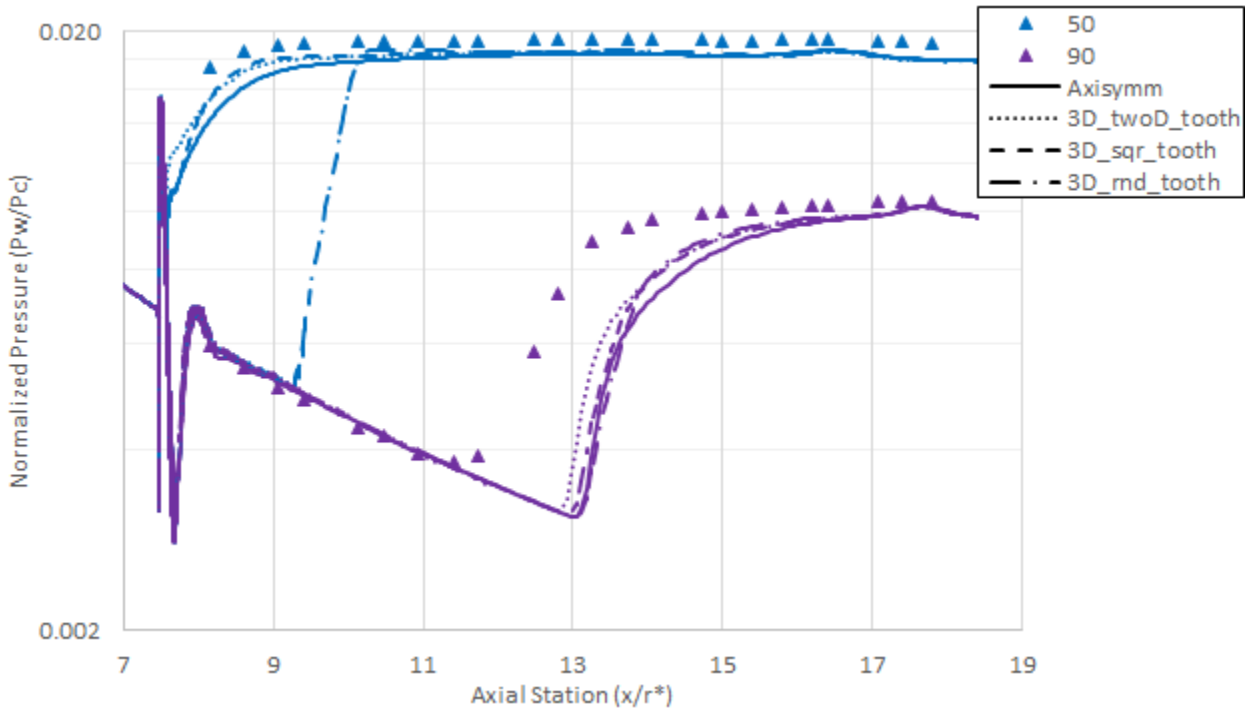

Figure 9. Non-dimensional pressure profiles at NPRs 50 and 90 for all mesh configurations (lines) using Menter's BSL model and Sarkar* compressibility correction plotted against the experimental results (symbols)

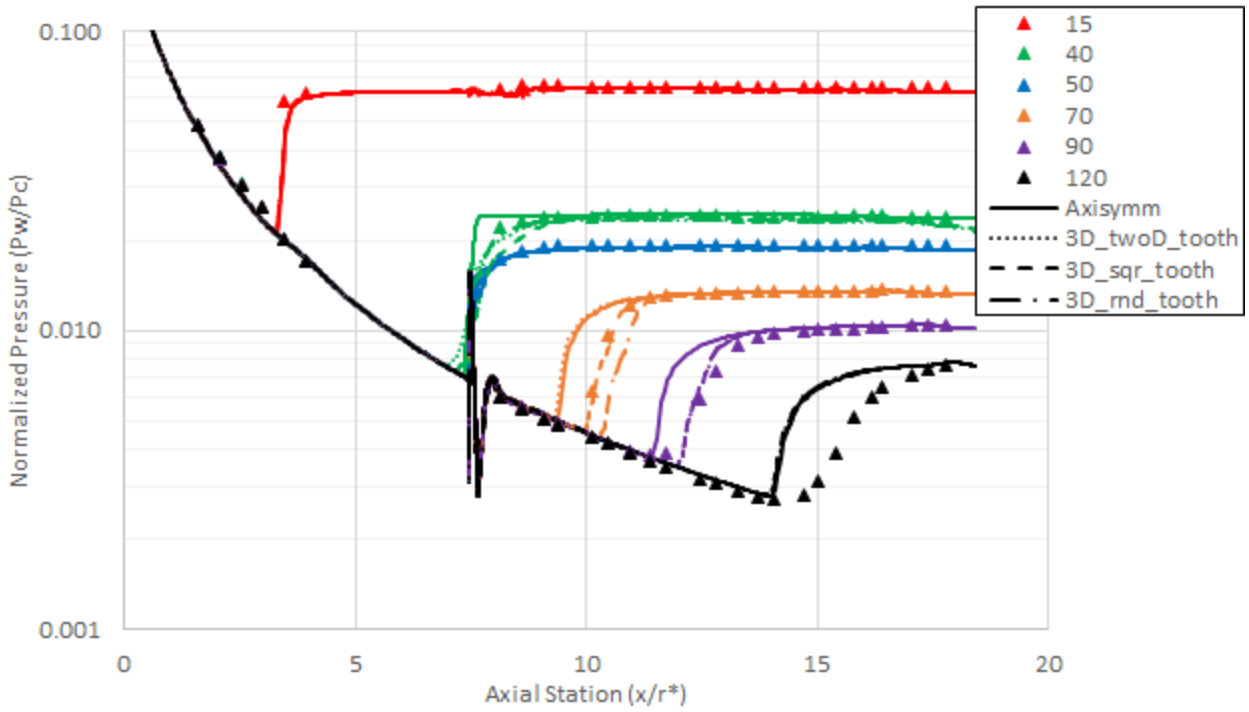

Figure 10. Non-dimensional pressure profiles at various NPR for all mesh configurations (lines) using Menter's BSL model and Wilcox compressibility correction plotted against the experimental results (symbols)

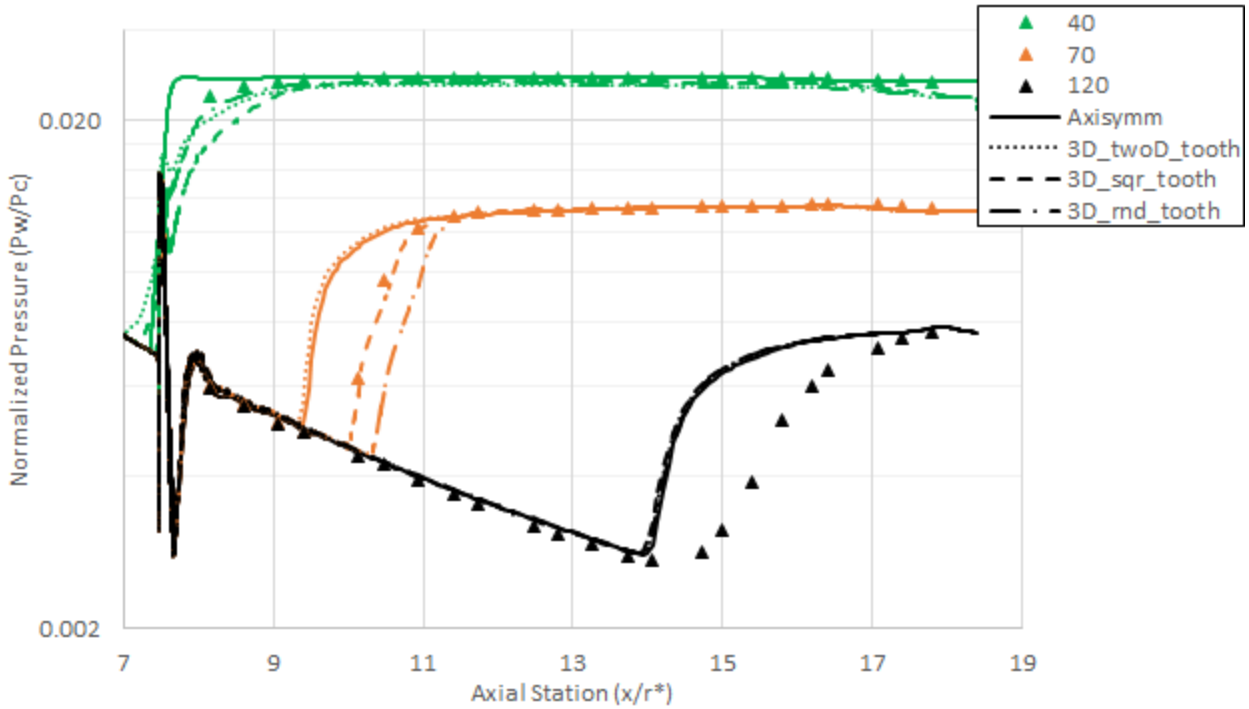

Figure 11. Non-dimensional pressure profiles at NPRs 40, 70, and 120 for all mesh configurations (lines) using Menter's BSL model and Wilcox compressibility correction plotted against the experimental results (symbols)

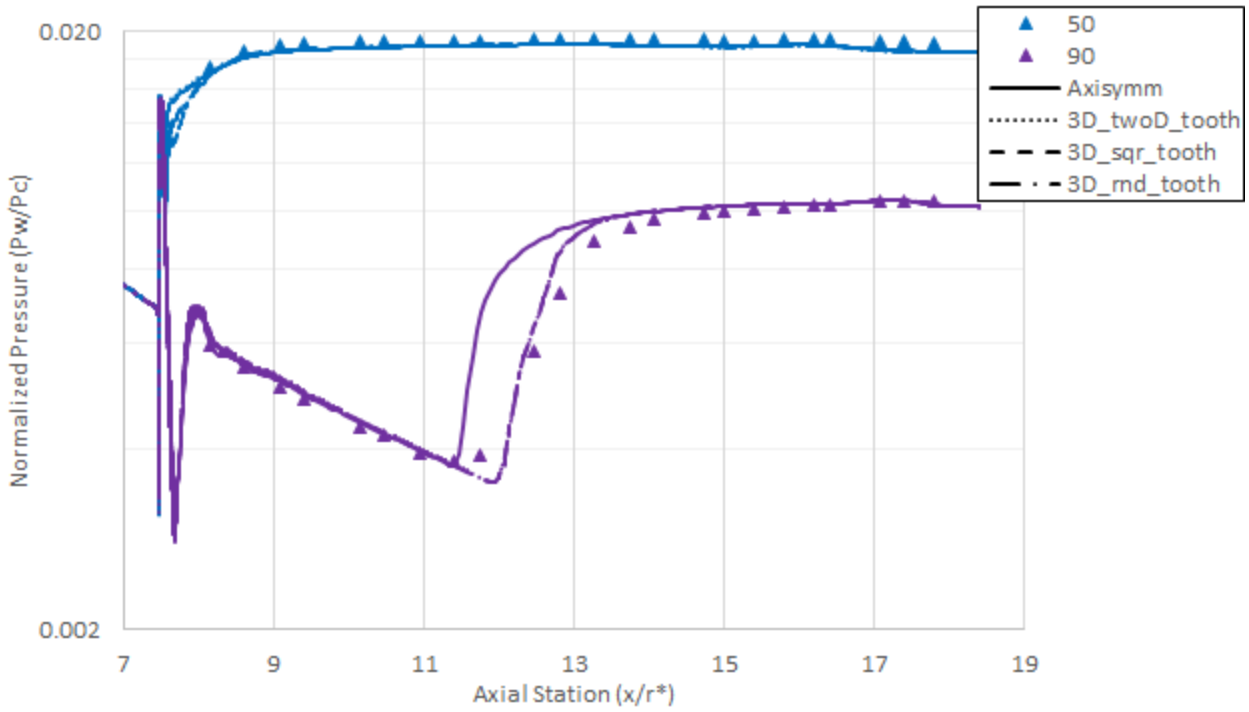

Figure 12. Non-dimensional pressure profiles at NPRs 50 and 90 for all mesh configurations (lines) using Menter's BSL model and Wilcox compressibility correction plotted against the experimental results (symbols)

IV. Conclusions

An axisymmetric model and a set of three three-dimensional models were generated to approximate the film cooling orificing geometry in a truncated ideal contour nozzle. The axisymmetric model was tested with a set of two turbulence models and two turbulent compressibility corrections to determine how each combination performed for the nozzle with and without film coolant flow. The results from those four combinations showed that Menter's Baseline model matched a set of experimental results previously obtained at the NASA MSFC Nozzle Test Facility better than Menter's Shear Stress Transport model. The results also showed that the nozzle flow separation location results of the two compressibility correction options, a modified version of the Sarkar correction and the Wilcox correction, tended to bound the experimental separation location. Therefore, Menter's Baseline turbulence model and both compressibility corrections were used for the three-dimensional configurations.

The results from all four configurations, the axisymmetric and the three three-dimensional configurations, were compared to each other and to the set of experimental results to determine the sensitivity of the nozzle wall pressures and flow separation location to the simplifications applied to the film injection geometry. For both the modified Sarkar and Wilcox compressibility correction options, the axisymmetric equivalent area slot geometry matches within 0.3 r* for separation location its three-dimensional equivalent (3D_twoD_tooth) for all simulated nozzle pressure ratios (NPRs). Thus the results show only a minor difference by treating the equivalent area slot case with a three-dimensional mesh. The simulations involving the two meshes with three-dimensional features, the squared-off tooth representation (3D_sqr_tooth) and the rounded tooth representation (3D_rnd_tooth), generally match the equivalent slot area configurations at low and high NPRs. For both compressibility corrections, the results exhibit flow separations further downstream for NPRs 70 and 90 than the equivalent slot area cases. For the Wilcox correction, this leads to a closer match to the rising pressures just downstream of separation.

With the modified Sarkar correction, for the NPRs with separation downstream of the nozzlette, the axisymmetric equivalent model matches closer with the experimental data than the models with three-dimensional nozzlette features. For the Wilcox correction, the models with three-dimensional nozzlette features show a closer match with the experimental data at two NPRs, but not for all of the NPRs. Therefore, improving the geometric fidelity of the nozzlette orificing does not necessarily result in the 'correct' flow separation locations. Other modeling applied in the simulations, for example the turbulence modeling, may lack the fidelity to fully characterize the separation in the nozzle.

Generally, while the exact positions of the nozzle flow separation cannot be predicted by these simulations, the surface pressures and separation locations can be predicted reasonably well. The separation locations lie within approximately one nozzle throat radius, r*, of the experimental results. The results for each mesh configuration typically show one NPR at which the simulation's separation location matches the experiment, while lower NPRs show late separation and higher NPRs show early separation. Additionally, for most NPRs and mesh configurations, the surface pressure profiles downstream of the separation location match the experimental pressure profiles closely.

References:

[1]Martelli, E., F. Nasuti, and M. Onofri, "Film Cooling Effect on Dual-Bell Nozzle Flow Transition," AIAA Paper 2009-4953, Aug. 2009.

[2]J. Ruf, D. McDaniels, and A. Brown, "Cold flow test results for nozzle side loads for J-2X and SSME test articles," JANNAF 2010.

[3]J. Ruf, D. McDaniels, and A. Brown, "Cold flow test results for the effect of supersonic film cooling on a truncated ideal contour's nozzle side loads," JANNAF 2010.

[4]E. Luke, X-L. Tong, J. Wu, L. Tang, and P. Cinnella, "A Step Towards `Shape Shifting'Algorithms: Reacting Flow Simulations Using Generalized Grids," *39th AIAA Aerospace Sciences Meeting and Exhibit*, January 8-11, 2001, Reno, NV, AIAA Paper 2001-0897.

[5]Q. Liu, E. Luke, and P. Cinnella, "Coupling Heat Transfer and Fluid Flow Solvers for Multi-Disciplinary Simulations," *AIAA Journal of Thermophysics and Heat Transfer*, Vol. 19, No. 4, Oct.-Dec. 2005, pp 417-427.

[6]J. Wu, L. Tang, E. Luke, "A Low Mach Number Preconditioning Scheme of the Reactive Roe Flux," *41st AIAA Aerospace Sciences Meeting and Exhibit*, January 6-9th, 2003, Reno, NV, AIAA Paper 2003-0307.

[7]E. Luke, "A Rule-Based Specification System for Computational Fluid Dynamics," Ph.D. Dissertation, Mississippi State University, December, 1999.

[8]E. Luke and T. George, "Loci: A Rule-Based Framework for Parallel Multidisciplinary Simulation Synthesis," *Journal of Functional Programming*, Special Issue on Functional Approaches to High-Performance Parallel Programming, Volume 15, Issue 03, 2005, pp. 477-502, Cambridge University Press.

[9]Menter, F.R., "Zonal Two Equation k-w Turbulence Models for Aerodynamic Flows," AIAA Paper 93-2906, July 1993.

[10]Menter, F.R., "Two-Equation Eddy-Viscosity Turbulence Models for Engineering Applications," *AIAA Journal*, Vol. 32, No. 8, Aug. 1994, pp. 1598-1605.

[11]Wilcox, D.C., *Turbulence Modeling for CFD*, DCW Industries, 1998.

[12]Sarkar, S. and Lakshmanan, B., "Application of a Reynolds Stress Turbulence Model to the Compressible Shear Layer," *AIAA Journal*, Vol. 29, No. 5, May 1991, pp. 743-749.